iScience

Article

Efficient ternary organic solar cells with suppressed nonradiative recombination via B−N based polymer donor

Graphical abstract

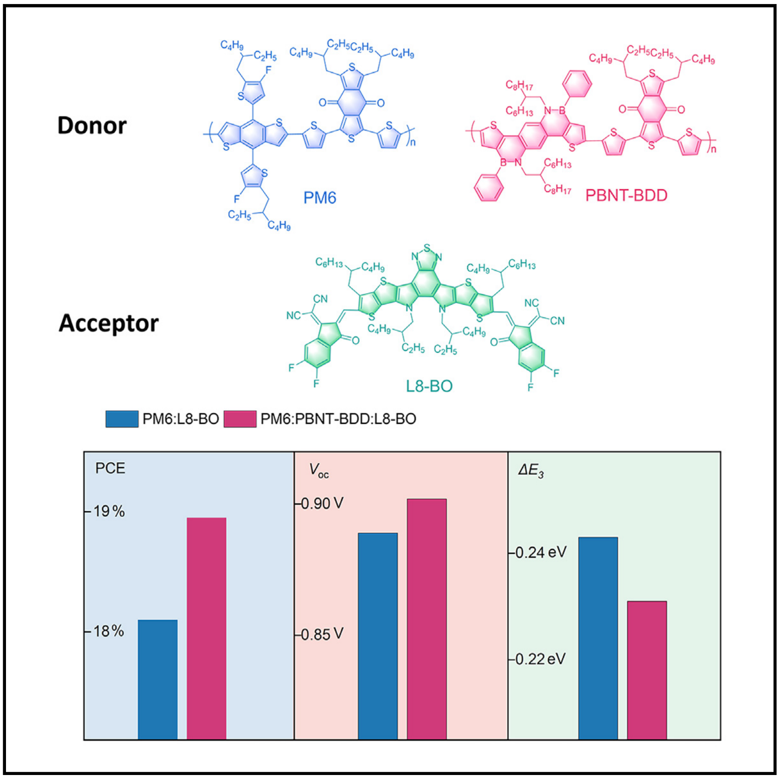

Highlights

- The B−N-based polymer donor processes high $E(T_1)$ and small ΔE_{ST} characters
- PBNT-BDD was incorporated into the PM6:L8-BO to construct ternary OSCs
- The ternary OSCs afford an impressive PCE of 18.95%
- The E_{loss} was reduced from 0.567 *eV* to 0.525 *eV*

Authors

Shuting Pang, Wanyuan Deng, Langheng Pan, ..., Jiayuan Zhu, Wensheng Yan, Chunhui Duan

Correspondence

pangshuting@hdu.edu.cn (S.P.),
wensheng.yan@hdu.edu.cn (W.Y.),
duanchunhui@scut.edu.cn (C.D.)

In brief

Materials science; Materials application; Devices

Pang et al., 2025, iScience *28*, 111682
January 17, 2025
https://doi.org/10.1016/j.isci.2024.111682

CellPress

CellPress
OPEN ACCESS

Article

Efficient ternary organic solar cells with suppressed nonradiative recombination via B−N based polymer donor

Shuting Pang,[1,5,6,*] Wanyuan Deng,[2,5] Langheng Pan,[2] Xinyuan Liu,[2] Zhibang Shen,[3] Hongxiang Li,[4] Pei Cheng,[4] Jiayuan Zhu,[4] Wensheng Yan,[1,*] and Chunhui Duan[2,*]

[1]Institute of Carbon Neutrality and New Energy, School of Electronics and Information Engineering, Hangzhou Dianzi University, Hangzhou 310018, China

[2]Institute of Polymer Optoelectronic Materials and Devices, State Key Laboratory of Luminescent Materials and Devices, South China University of Technology, Guangzhou 510640, China

[3]Institute of High Energy Physics, Chinese Academy of Sciences, Beijing 100049, P.R. China

[4]College of Polymer Science and Engineering, State Key Laboratory of Polymer Materials Engineering, Sichuan University, Chengdu 610065, China

[5]These authors contributed equally

[6]Lead contact

*Correspondence: pangshuting@hdu.edu.cn (S.P.), wensheng.yan@hdu.edu.cn (W.Y.), duanchunhui@scut.edu.cn (C.D.)

https://doi.org/10.1016/j.isci.2024.111682

SUMMARY

Organic solar cells (OSCs) have developed rapidly in recent years. However, the energy loss (E_{loss}) remains a major obstacle to further improving the photovoltaic performance. To address this issue, a ternary strategy has been employed to precisely tune the E_{loss} and boost the efficiency of OSCs. The B−N-based polymer donor has been proved to process high $E(T_1)$ and small ΔE_{ST} characters, which can inhibition of CT state recombination. Herin, B−N-based polymer donor PBNT-BDD was incorporated into the state-of-the-art PM6:L8-BO binary to construct ternary OSCs. Together with the optimal morphology, the ternary device affords an impressive power conversion efficiency of 18.95% with an improved open-circuit voltage (V_{oc}), short-circuit density (J_{sc}), and reduced E_{loss} in comparison to the binary ones, which is the highest PCE for B−N materials-based ternary device. This work broadens the selection of guest materials toward realizing the high performance of OSCs.

INTRODUCTION

Solution-processed organic solar cells (OSCs) have attracted considerable attention as a promising future photovoltaic technology because of their many benefits, including being able to be processed in solution, lightweight, and transparent.[1–4] In recent years, significant progress has been made in the development of nonfullerene acceptors and polymer donors, along with a more comprehensive understanding of device engineering. As a result, single-junction organic solar cells (OSCs) have achieved power conversion efficiencies (PCE) exceeding 19%.[5–22] The peak external quantum efficiencies (EQE) and fill factor (FF) for organic solar cells have surpassed 80%. However, the open-circuit voltage (V_{oc}) still falls significantly below the predictions of the Shockley–Queisser theory.[23] The low voltage or high voltage loss imposes a limitation on the power conversion efficiency (PCE) of organic solar cells. The V_{oc} is mainly affected by the energy level and E_{loss}. Many studies have suggested that lowering the HOMO level of donor materials and increasing the LUMO level of acceptors can potentially enhance the V_{oc} upper limit.[24] To further improve the V_{oc} values of OSCs, it is essential to reduce the energy loss. The E_{loss} can be expressed a $E_{loss} = E_g - qV_{oc} = (qE_g - qV_{oc}^{SQ}) + q\Delta V_{oc}^{rad,below\ gap}) + qV_{oc}^{non-rad} = \Delta E_1 + \Delta E_2 + \Delta E_3$ (*Equation* 1).[25,26] The ΔE_1 is associated with radiative recombination originating from absorption above the bandgap, which represents an unavoidable loss for all types of solar cells and typically falls within the range of 0.25–0.30 eV.[19,20] The ΔE_2 arises from additional radiative recombination resulting from absorption below the bandgap. The significant ΔE_2 is attributed to the presence of charge transfer (CT) states, which have lower energy levels than the bandgap, leading to a redshifted absorption. ΔE_2 is an intrinsic loss in solar cells and is closely linked to both the local excited (LE) state and CT state in OSCs.[27] The difference between LE and CT states is related to the driving force for exciton dissociation. However, it has been demonstrated that donor/non-fullerene acceptor pair-based OSCs can still achieve fast and efficient charge dissociation even with low driving force, resulting in superior PCEs with improved V_{oc}. In a word, ΔE_2 is not the primary factor influencing energy loss and device V_{oc}. However, in comparison to silicon and perovskite solar cells, the larger nonradiative recombination (ΔE_3) poses a significant challenge in limiting the further enhancement of OSC performance.[28–31]

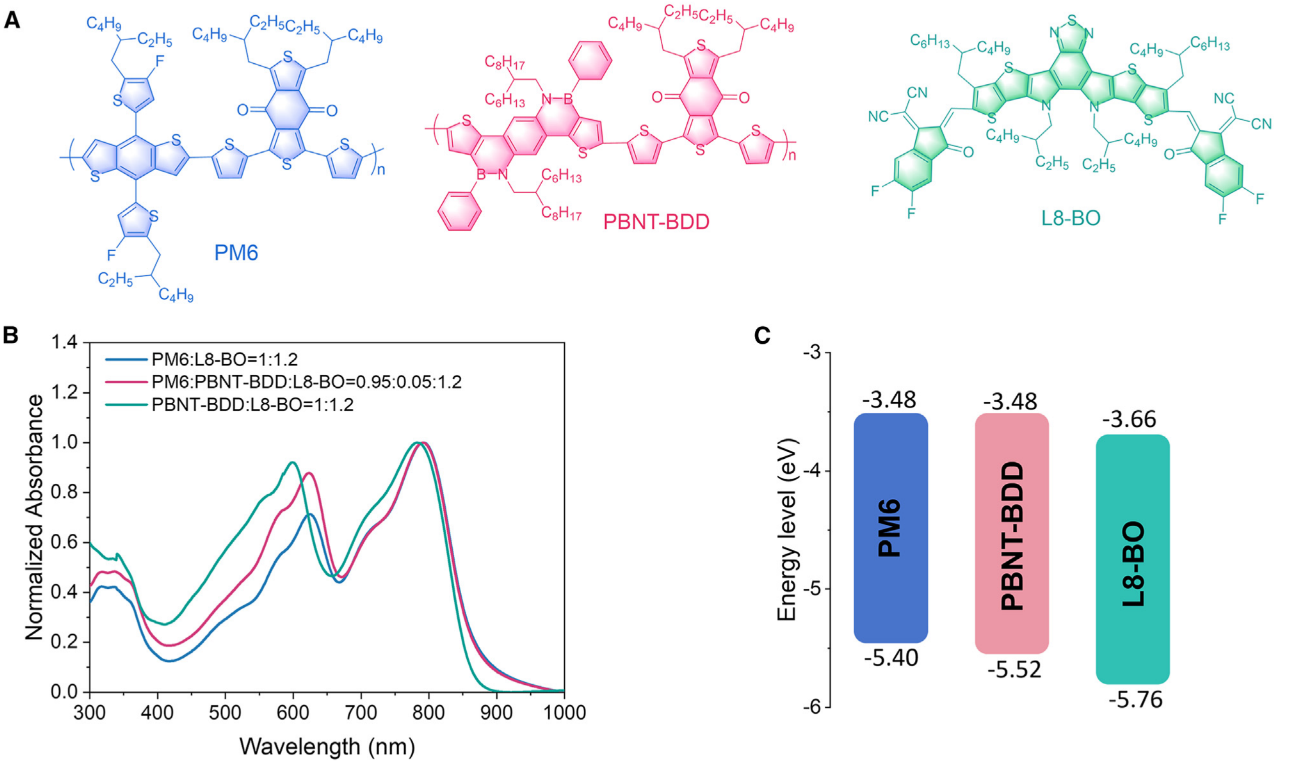

Figure 1. Chemical structure and basic characters of PM6, PBNT-BDD and L8-BO

(A) Chemical structure of the host donor PM6, the guest donor PBNT-BDD, and acceptor L8-BO.

(B) The UV-vis absorption spectra of blend films.

(C) The energy diagram of polymers and acceptor.

Incorporating a third component to form a ternary blend has been proven as a general strategy to explore more possibilities in addressing the a fore mentioned energy loss issues, thereby offering a convenient approach to enhance the V_{oc} of OPVs. Additionally, introducing the third component can maintain the appropriate morphology of an efficient binary system, leading to improved device performance.[32–34] The guest component can gradient adjust the energy level of the device and enhance the absorption of the light-harvesting spectrum. Furthermore, it is important that the introduced guest component is compatible with either the donor or acceptor in the host binary system, in order to facilitate the formation of a suitable BHJ microstructure for efficient photoelectric conversion.

Here, we report an efficient ternary OSC by introducing a B−N based polymer PBNT-BDD into PM6:L8-BO.[35] As "D-A" type polymer donors, PBNT-BDD possess the same "A" unit of PM6, in which ensures the good compatibility with the host donor PM6. Impressively, PBNT-BDD exhibits a wider bandgap, which can enhance the absorption of the device at high band gap. Additionally, the PBNT-BDD possesses more deeper HOMO energy level, which is beneficial to obtain higher V_{oc}. Importantly, B–N based polymer PBNT-BDD process high E(T_1) and small ΔE_{ST} characters due to the opposite resonance effect of B and N atoms, which can inhibit CT state recombination. The CT state recombination is one of the main ways of non-radiative recombination loss.[36–38] As a result, the top-performing ternary OSCs device demonstrates a high PCE of 18.95%, which is attributed to the simultaneous improvements in V_{oc} and J_{sc}. This study further broadens the potential applications of boron-nitrogen covalent bond materials in the field of organic photovoltaics and offers insights for the continued development and utilization of new materials.

RESULTS AND DISCUSSION

The chemical structure of donors PM6 and PBNT-BDD, and acceptor L8-BO are shown in Figure 1A. The ultraviolet–visible–near-IR (UV–vis–NIR) spectroscopy of pure films of PM6, PBNT-BDD, and L8-BO is shown in Figure S1. Compared to PM6, the PBNT-BDD film exhibits a blue-shift, with absorption peaks at 600 nm and 550 nm. As depicted in Figure 1B, the incorporation of PBNT-BDD into the PM6:L8-BO binary blend can significantly enhance the light-harvesting capability of the active layer up to 620 nm. Additionally, cyclic voltammetry (CV) measurements were carried out to evaluate the energy levels of relevant materials (Figure S2). The acceptor L8-BO exhibited HOMO and LUMO energy levels of -3.66/–5.76 eV. In comparison, the neat PBNT-BDD donor demonstrated a deeper HOMO energy level of -5.52 eV, as opposed to the -5.40 eV HOMO energy level for PM6 (Figure 1C). A deeper HOMO energy level can contribute to achieving a higher V_{oc} for the device.[39]

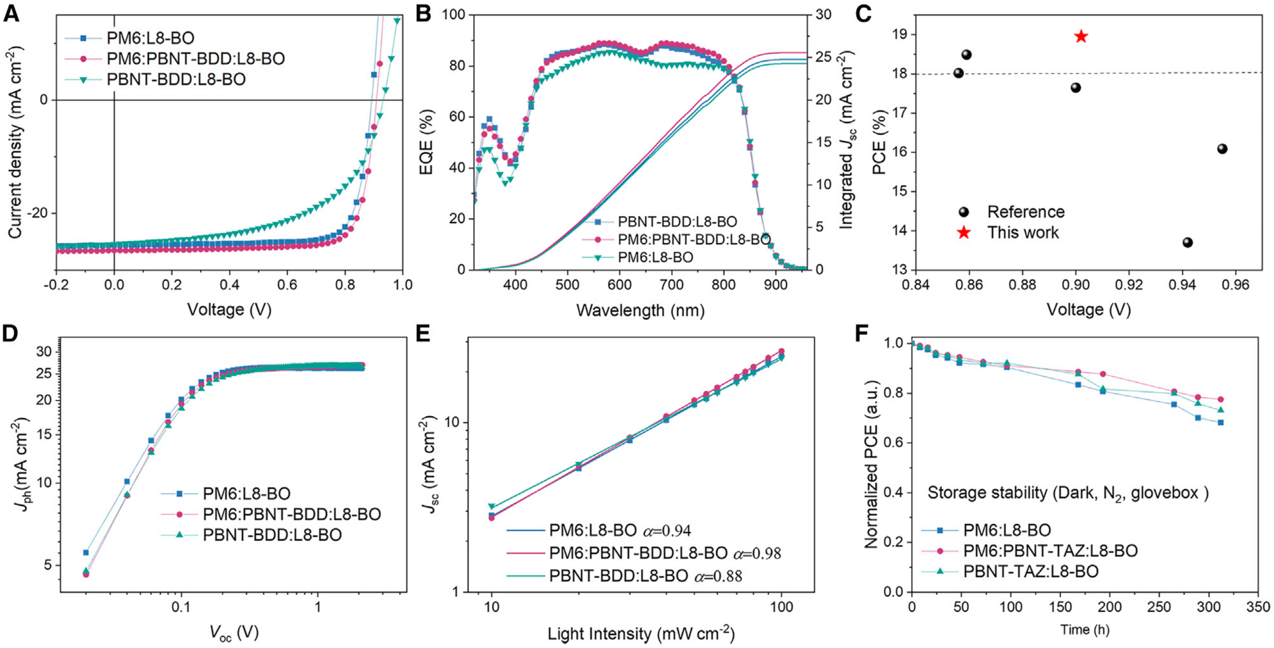

Figure 2. Photovoltaic performance of OSCs devices

(A) The J–V curves and (B) EQEs spectra of devices.

(C) The V_{oc} values of efficient OSCs with PCEs.

(D) The dependence of the J_{sc} on the light intensity for the optimum devices.

(E) The plots of the photocurrent density versus effective voltage.

(F) Storage stability of unsealed OSCs under dark ambient conditions (dark, glovebox, 25°C).

Considering that the PM6 and PBNT-BDD have the same "A" unit, it is possible that the two polymer donors have good compatibility to form an alloy-like phase in ternary blend films. To confirm the formation of alloy states between PM6 and PBNT-BDD, contact angle measurements were carried out to assess the compatibility between the two materials (Figure S3). According to the Owens's law,[40] the surface tension (γ) of PM6, PBNT-BDD, and L8-BO is calculated to be 18.38, 19.04, and 23.11 mN m^{-1}, respectively. The Flory–Huggins interaction parameter χ can be evaluated the miscibility between two components in a blend using the equation $\chi_{AB} = \kappa\left(\sqrt{\gamma_A} - \sqrt{\gamma_B}\right)^2$.[41] The calculated $\chi_{\text{PM6:PBNT-BDD}}$ is 0.00582k mN m^{-1}, which is significantly smaller than those of $\chi_{\text{PM6:L8-BO}}$ (0.271k) and $\chi_{\text{PBNT-BDD:L8-BO}}$ (0.197k). This indicates that the two donors are miscible into a donor alloy in ternary blend films. This property can mainly maintain the morphology of the original PM6:L8-BO and reduce the difficulty of morphology optimization.

Device performance

Devices were fabricated using a conventional architecture of indium tin oxide (ITO)/poly(3,4-ethylenedioxythiophene): poly(styrene sulfonate) (PEDOT:PSS)/active layer/PNDIT-F3N/Ag with a fixed D/A weight ratio of 1:1.2 dissolved in chloroform solution with 50% additive of 1, 4-diiodobenzene by weight. Thermal annealing was conducted at 90°C for 5 min. The representative current density–voltage (J–V) curves of the optimal binary and ternary devices under the AM 1.5G solar simulator are exhibited in Figure 2A, and the corresponding photovoltaic parameters are summarized in Table 1. The PM6:L8-BO based binary device demonstrates a PCE of 18.10%, with a V_{oc} of 0.889 V, a J_{sc} of 25.59 mA cm^{-2}, and an FF of 79.57%. The performance of the PM6:L8-BO device is comparable to the reported data in existing literature.[42] For the PBNT-BDD:L8-BO device, a high V_{oc} of 0.930 V and a J_{sc} of 25.39 mA cm^{-2} was obtained, but the low FF limits the PCE of device, which may be due to the amorphous crystalline character of PBNT-BDD. The J–V curves and device parameters of ternary devices with different PBNT-BDD contents are summarized in Table S2. By incorporating 5 wt % PBNT-BDD into PM6:L8-BO blend, the best PCE of 18.95% was obtained with a V_{oc} of 0.902 V and a J_{sc} of 26.54 mA cm^{-2}. The corresponding external quantum efficiency (EQE) curves are depicted in Figure 2B and the EQE curves are in good agreement with the results from J-V measurements. (Table 1). Notably, the EQE values of the ternary devices demonstrate a heightened response at 550 nm, which corresponds to the absorption spectrum. The incorporation of PBNT-BDD not only elevates the device V_{oc} and expands the absorption range and EQE response but also preserves the favorable morphology of the original binary system with minimal additional content. Consequently, there is an enhancement in device efficiency. With an increasing adding ratio, V_{oc} further improves, but FF drops significantly. This phenomenon may be due to poor morphology in the PBNT-BDD:L8-BO system. After investigation, the PCE of 18.95% is the reported highest PCE of boron-nitrogen containing material based ternary devices. We

Table 1. The photovoltaic parameters of OSCs based on binary and ternary devices

Device[a]	V_{oc} (V)	J_{sc} (mA cm^{-2})	J_{sc} (EQE)[b] (mA cm^{-2})	FF (%)	PCE (%)
PM6:L8-BO	0.889 (0.882 ± 0.10)	25.59 (25.45 ± 0.15)	24.82	79.57 (79.40 ± 0.35)	18.10 (17.96 ± 0.14)
PM6:PBNT-BDD:L8-BO	0.902 (0.895 ± 0.010)	26.54 (26.30 ± 0.25)	25.61	79.18 (78.65 ± 0.60)	18.95 (18.75 ± 0.20)
PBNT-BDD:L8-BO	0.930 (0.925 ± 0.006)	25.39 (25.24 ± 0.15)	24.33	55.87 (55.75 ± 0.30)	13.20 (13.00 ± 0.20)

[a] The Table contain the best photovoltaic parameters of OSCs and average values.

[b] The data were calculated by integrating the EQE.

also evaluated the storage stability of the devices. It was observed that the inclusion of a small amount of PBNT-BDD in the binary host blend can promote the storage stability of the device. After 300 h, the ternary device retained 78% of its original PCE, while the PCE of the PM6:L8-BO and PBNT-TAZ:L8-BO devices decreased to 68% and 73%, respectively. PBNT-BDD offered better device storage stability than PM6, and the result is consistent with the literature report.[35] We further tested the unencapsulated devices in maximum power point tracking (MPPT) mode under 1-sun illumination in an N_2 atmosphere to assess their long-term operating stability (Figure S4). The PCE of PM6:L8-BO dropped to 67% of its initial PCE after 250 h. In comparison, the ternary device maintained 77% of the original PCE under the same condition. For the thermal stability test, the ternary device also shows better thermal stability than the PM6:L8-BO device. The enhanced stability of ternary devices may stem from the optimized phase separation and the detailed morphologies will be discussed later.

Charge generation, transport, and recombination

To investigate the impact of PBNT-BDD on the process of charge generation and dissociation, we conducted measurements of the photocurrent density (J_{ph}) as a function of effective voltage (V_{eff}), as shown in Figure 2D. The J_{ph} reaches a saturation value (J_{sat}) with saturation values of 23.46, 25.40, and 22.53 mA cm^{-2} for PM6:L8-BO, PM6:PBNT-BDD:L8-BO, and PBNT-BDD:L8-BO blends, respectively. Furthermore, we used the exciton dissociation probability P(E,T) as an indicator for exciton dissociation and charge collection efficiency, which P(E,T) is determined as J_{ph}/J_{sat}.[43] The ternary device exhibited higher P(E,T) values, indicating that the introduction of PBNT-BDD both contributed to efficient exciton dissociation and charge extraction properties. Using the space-charge limited current (SCLC) method, measurements of carrier mobilities were conducted for three systems (Figure S7; Table S4). The comparison of the more balanced hole and electron mobilities in the ternary system ($\mu_e/\mu_h = 1.04$) with those of the two binary systems (1.07 for PM6:L8-BO and 1.10 for PBNT-BDD:L8-BO, respectively) suggests that charge carriers can be transmitted more efficiently in the ternary devices. This indicates a potential advantage for utilizing ternary systems in electronic applications. The charge recombination kinetics of charge recombination in both binary and ternary devices were investigated. The J_{sc} versus light intensity (P_{light}) is plotted in Figure 2C. The relationship between J_{sc} and P_{light} can be defined as $J_{sc} \propto P_{light}{}^{\alpha}$, where α represents the extent of bimolecular charge recombination. A higher α value generally indicates lower bimolecular recombination losses.[44] As illustrated in Figure 2C, the α value increases from 0.94 (PM6:L8-BO) and 0.88 (PBNT-BDD:L8-BO) to 0.98 (PM6:PBNT-BDD:L8-BO). Therefore, an appropriate amount of PBNT-BDD leads to a reduction in recombination losses.

Energy loss analysis

Further detailed analyses were conducted to examine the energy loss (E_{loss}) for the PM6:L8-BO, PM6:PBNT-BDD:L8-BO, and PBNT-BDD:L8-BO devices (Figure 3). The purpose of the analysis was to investigate the impact of PBNT-BDD incorporation on the three components of E_{loss} (ΔE_1, ΔE_2, ΔE_3), with corresponding values summarized in Table 2. The E_g was calculated as half of EQE$_{max}$ point,[45] resulting in blend film values of 1.456, 1.455, and 1.455 *eV* respectively. By combining this data with $V_{oc}{}^{cal}$ data, the E_{loss} values were determined to be 0.571 *eV* for PM6:L8-BO, 0.557 *eV* for PM6:PBNT-BDD:L8-BO, and 0.525 *eV* for PBNT-BDD:L8-BO. The presence of ΔE_1 was unavoidable in these systems, ranging from an observed value of between 0.265 and 0.266 *eV*. The ΔE_2 values are calculated as 0.062 *eV*, 0.057 *eV,* and 0.058 *eV* for the PM6:L8-BO, PM6:PBNT-BDD:L8-BO and PBNT-BDD:L8-BO device, respectively, indicative of the slightly reduced reorganization energy or energetic disorder in the ternary device. ΔE_3 is commonly caused by bimolecular and trap-assisted recombination. It is calculated by the following equation: $\Delta E_3 = -KT \ln(\mathrm{EQE}_{EL})$, where EQE$_{EL}$ is electroluminescence external quantum efficiency. The ΔE_3 of PM6:L8-BO, PM6:PBNT-BDD:L8-BO, and PBNT-BDD:L8-BO devices are 0.243, 0.235 and 0.216 *eV*, respectively (Table 2). Benefit from the high $E(T_1)$ and small ΔE_{ST} characters of PBNT-BDD, the PBNT-BDD based device has been proved process small ΔE_3 by reducing CT state recombination. Introducing the PBNT-BDD into PM6:L8-BO system, the ΔE_3 reduced from 0.243 *eV* of binary device to 0.235 *eV* of ternary device. The lower ΔE_3 contributes a higher V_{oc} in the PM6:PBNT-BDD:L8-BO device. Based on the above analysis, the improved V_{oc} of the ternary OSCs compared PM6:L8-BO binary device can be attributed to the reduced ΔE_3.

Morphology analysis

In order to gain a deeper understanding of the modified photovoltaic characteristics in the ternary devices, we utilized atomic force microscopy (AFM) measurements to analyze the surface morphology. As shown in Figure 4A, it is evident that the images and root-mean-square (RMS) roughness of the

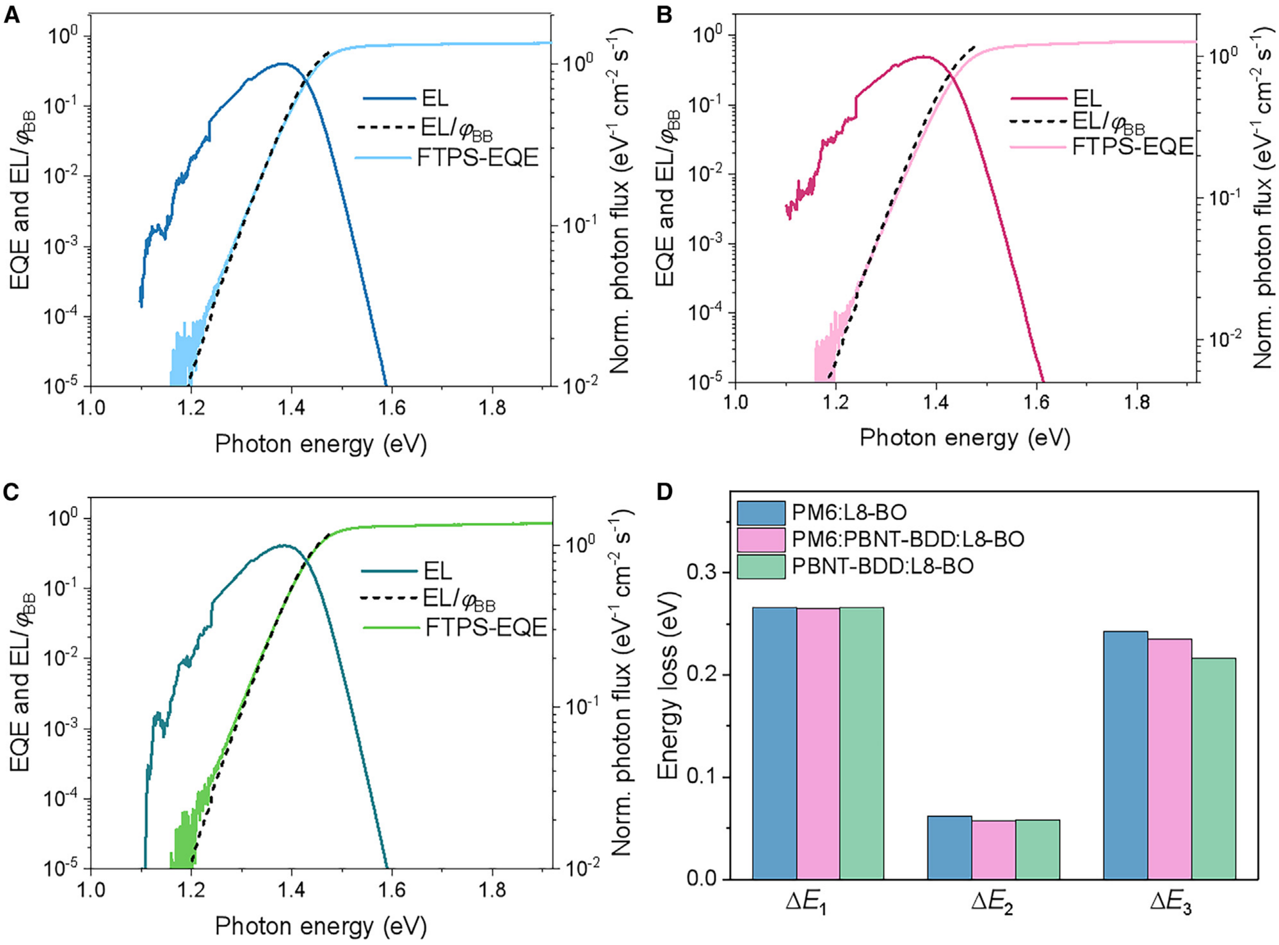

Figure 3. E_{loss} data analysis of OSCs devices

The measured EL spectrum and experimental EQE spectrum used to determine $V_{oc,Rad}$ for the devices.
(A) PM6:L8-BO, (B) PM6:PBNT-BDD:L8-BO, (C) PBNT-BDD:L8-BO, (D) detailed energy losses of devices.

blends exhibit distinct differences. This can be attributed to the strong crystallizable of PM6 and the amorphous character of PBNT-BDD, leading to different morphologies in binary blend films. Besides, the $\chi_{\text{PBNT-BDD:L8-BO}}$ (0.197*k*) is larger than $\chi_{\text{PM6:L8-BO}}$ (0.271*k*), indicating that PBNT-BDD and L8-BO have stronger miscibility, thus the PBNT-BDD:L8-BO film shows smaller RMS. Moreover, in comparison to the PM6:L8-BO binary blend, it is observed that the ternary blend PM6:PBNT-BDD:L8-BO showed a lower RMS value of 1.27 nm. The results indicated that PBNT-BDD can fuse well with the active layer, which is consistent with the contact angle measurement results.

The molecular ordering and packing behavior of the pure films and blend films were investigated by using GIWAXS measurements.[46] It was found that PM6 and L8-BO exhibit a strong (010) diffraction peak in the out-of-plane (OOP) direction and an (100) diffraction in the in-plane (IP) direction, indicating a tendency toward a face-on orientation. On the other hand, PBNT-BDD prefers an amorphous state. In terms of the blend films, the 2D patterns of the PM6:L8-BO and PM6:PBNT-BDD:L8-BO blends indicate similar face-on-oriented molecular packing, which suggests that the addition of PBNT-BDD to the PM6:L8-BO has little effect on the orientation of the blended film. The crystal coherence lengths (CCLs) were calculated using the

Table 2. Total and detailed energy losses of binary and ternary OSCs

Active layer	E_g (eV)	V_{oc}^{cal} (eV)	E_{loss} (eV)	ΔE_1 (eV)	ΔE_2 (eV)	EQE_{EL}	ΔE_3 (eV)
PM6:L8-BO	1.456	0.885	0.571	0.266	0.062	7.79×10^{-5}	0.243
PM6:PBNT-BDD:L8-BO	1.455	0.898	0.557	0.265	0.057	1.06×10^{-4}	0.235
PBNT-BDD:L8-BO	1.455	0.915	0.540	0.266	0.058	2.22×10^{-4}	0.216

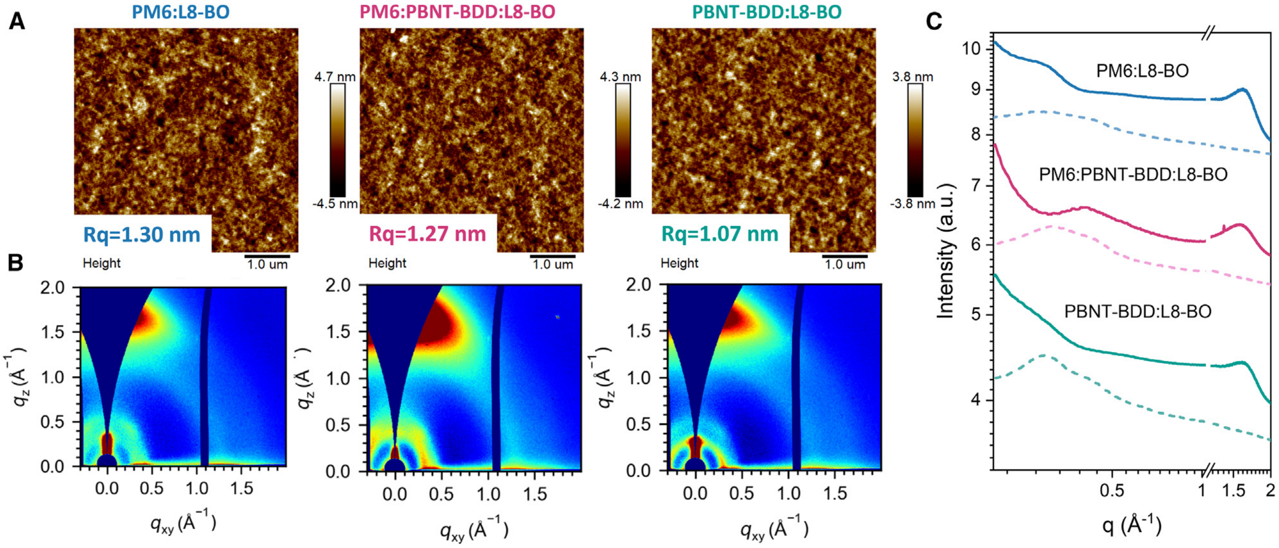

Figure 4. Morphology characterizations of blends

(A) Tapping-mode AFM height images. The scan area and step size of Raman mapping are 5 μm × 5 μm and 0.1 μm, respectively.

(B) 2D GIWAXS patterns and (C) 1D line-cut profiles in out-of-plane and in-plane directions of the blend films.

formula CCL = 0.9 ×(2π/FWHM) (Å),[46] where FWHM is the full width at half-maximum of the corresponding diffraction peak, as summarized in Table S5 from fitting 1D line cuts with multiple peaks fitting. In addition, the CCL value of the ternary blend was 20.67 Å, and the (010) peak is located at q_z = 1.74 Å^{-1}, corresponding to a π–π stacking distance of 3.61 Å, which showed improvement compared to the PM6:L8-BO ternary blend (15.09 and 3.69 Å respectively). These results indicate that adding low crystalline donor PBNT-BDD induces a higher degree of molecular packing, resulting in enhanced charge transport and suppressed carrier recombination.

In conclusion, high-performance ternary OSCs were prepared using PM6:L8-BO as the host system and PBNT-BDD as the guest donor. The inclusion of PBNT-BDD expanded the optical absorption range and optimized molecular packing and phase separation in the ternary films. Additionally, PBNT-BDD processes high E(T_1) and small ΔE_{ST} characters due to the opposite resonance effect of B and N atoms, which can inhibit CT state recombination and reduce energy loss. As a result, the ternary OSCs achieved a higher PCE of 18.95%, with an increased J_{sc} of 26.54 mA cm^{-2}, V_{oc} of 0.902 V, and FF of 79.18% compared to that of the PM6-based binary OSCs. Furthermore, we observed reduced E_{loss} and ΔE_3 in the ternary device in the PM6:PBNT-BDD:L8-BO device. This illustrates that strategically introducing high E(T$_1$) and small ΔE_{ST} B−N based materials through donor gust strategy is an effective approach for achieving highly efficient OSCs.

Limitations of the study

For PL quenching measurements, the experiment of excitation acceptor L8-BO to detect the quenching efficiency of the donor has not been realized due to the limitation of the excitation wavelength of the equipment.

RESOURCE AVAILABILITY

Lead contact

Requests for further information and resources should be directed to and will be fulfilled by the lead contact, Associate Professor Shuting Pang (pangshuting@hdu.edu.cn).

Materials availability

This study did not generate new unique reagents. The readers can buy the chemicals to remake the materials as mentioned in the text.

Data and code availability

- Data: All data reported in this article will be shared by the lead contact upon request.
- Code: This article does not report the original code.
- Additional information: Any additional information required to reanalyze the data reported in this article is available from the lead contact upon request.

ACKNOWLEDGMENTS

The research was financially supported by the National Key Research and Development Program of China under Grant No.2022YFB4200904, National Natural Science Foundation of China No.22109046, Sichuan Science and Technology Program No.2023NSFSC0990 and Research Start-up Fund of Hangzhou Dianzi University No. KYS045623176. This work was carried out with the support of the Shanghai Synchrotron Radiation Facility (SSRF), beamline BL02U2. The authors thank SSRF BL02U2 for 2D GIWAXS measurements.

AUTHOR CONTRIBUTIONS

S.P. conceived the idea and performed the fabrication and characterization of the solar cells. W.D. performed energy loss measurements and data analysis. L.P. and X.Y. helped contact GIWAXS test. Z.S. and H.L. performed the GIWAXS measurements and data analysis under the guidance of P.C. and J.Z. W.Y. and C.D. helped with the project administration. S.P. prepared the article. All authors commented on the article.

DECLARATION OF INTERESTS

The authors declare no competing interests.

STAR★METHODS

Detailed methods are provided in the online version of this paper and include the following:

- KEY RESOURCES TABLE
- METHOD DETAILS
  - Device fabrication
  - Device characterization
- QUANTIFICATION AND STATISTICAL ANALYSIS

SUPPLEMENTAL INFORMATION

Supplemental information can be found online at https://doi.org/10.1016/j.isci.2024.111682.

Received: August 5, 2024
Revised: October 22, 2024
Accepted: December 20, 2024
Published: December 24, 2024

REFERENCES

1. Yu, G., Gao, J., Hummelen, J.C., Wudl, F., and Heeger, A.J. (1995). Polymer Photovoltaic Cells: Enhanced Efficiencies via a Network of Internal Donor-Acceptor Heterojunctions. Science *270*, 1789–1791. https://doi.org/10.1126/science.270.5243.1789.
2. Inganas, O. (2018). Organic Photovoltaics over Three Decades. Adv. Mater. *30*, 1800388. https://doi.org/10.1002/adma.201800388.
3. Liu, Y., Liu, B., Ma, C.Q., Huang, F., Feng, G., Chen, H., Hou, J., Yan, L., Wei, Q., Luo, Q., et al. (2022). Recent Progress in Organic Solar Cells (Part I material science). Sci. China Chem. *65*, 224–268. https://doi.org/10.1007/s11426-021-1180-6.
4. Liu, Y., Liu, B., Ma, C.Q., Huang, F., Feng, G., Chen, H., Hou, J., Yan, L., Wei, Q., Luo, Q., et al. (2022). Recent Progress in Organic Solar Cells (Part II device engineering). Sci. China Chem. *65*, 1457–1497. https://doi.org/10.1007/s11426-022-1256-8.
5. Lin, Y., Wang, J., Zhang, Z.G., Bai, H., Li, Y., Zhu, D., and Zhan, X. (2015). An Electron Acceptor Challenging Fullerenes for Efficient Polymer Solar Cells. Adv. Mater. *27*, 1170–1174. https://doi.org/10.1002/adma.201404317.
6. Yuan, J., Zhang, Y., Zhou, L., Zhang, G., Yip, H.L., Lau, T.K., Lu, X., Zhu, C., Peng, H., Johnson, P.A., et al. (2019). Single-Junction Organic Solar Cell with over 15% Efficiency Using Fused-Ring Acceptor with Electron-Deficient Core. Joule *3*, 1140–1151. https://doi.org/10.1016/j.joule.2019.01.004.
7. Li, C., Zhou, J., Song, J., Xu, J., Zhang, H., Zhang, X., Guo, J., Zhu, L., Wei, D., Han, G., et al. (2021). Non-fullerene Acceptors with Branched Side Chains and Improved Molecular Packing to Exceed 18% Efficiency in Organic Solar Cells. Nat. Energy *6*, 605–613. https://doi.org/10.1038/s41560-021-00820-x.
8. Wang, J., Wang, Y., Bi, P., Chen, Z., Qiao, J., Li, J., Wang, W., Zheng, Z., Zhang, S., Hao, X., and Hou, J. (2023). Binary Organic Solar Cells with 19.2% Efficiency Enabled by Solid Additive. Adv. Mater. *35*, 2301583. https://doi.org/10.1002/adma.202301583.
9. Guan, S., Li, Y., Xu, C., Yin, N., Xu, C., Wang, C., Wang, M., Xu, Y., Chen, Q., Wang, D., et al. (2024). Self-Assembled Interlayer Enables High-Performance Organic Photovoltaics with Power Conversion Efficiency Exceeding 20. Adv. Mater. *36*, 2400342. https://doi.org/10.1002/adma.202400342.
10. Zhu, L., Zhang, M., Xu, J., Li, C., Yan, J., Zhou, G., Zhong, W., Hao, T., Song, J., Xue, X., et al. (2022). Single-Junction Organic Solar Cells with over 19% Efficiency Enabled by a Refined Double-Fibril Network Morphology. Nat. Mater. *21*, 656–663. https://doi.org/10.1038/s41563-022-01244-y.
11. Zhang, Y., Deng, W., Petoukhoff, C.E., Xia, X., Lang, Y., Xia, H., Tang, H., Chandran, H.T., Mahadevan, S., Liu, K., et al. (2024). Achieving 19.4% Organic Solar Cell via An in Situ Formation of P-I-N Structure with Built-in Interpenetrating Network. Joule *8*, 509–526. https://doi.org/10.1016/j.joule.2023.12.009.
12. Liu, K., Jiang, Y., Ran, G., Liu, F., Zhang, W., and Zhu, X. (2024). 19.7% Efficiency Binary Organic Solar Cells Achieved by Selective Core Fluorination of Nonfullerene Electron Acceptors. Joule *8*, 835–851. https://doi.org/10.1016/j.joule.2024.01.005.
13. Zou, B., Wu, W., Dela Peña, T.A., Ma, R., Luo, Y., Hai, Y., Xie, X., Li, M., Luo, Z., Wu, J., et al. (2024). Step-by-Step Modulation of Crystalline Features and Exciton Kinetics for 19.2% Efficiency Ortho-Xylene Processed Organic Solar Cells. Nano-Micro Lett. *16*, 30. https://doi.org/10.1007/s40820-023-01241-z.
14. Zhang, C., Zhong, X., Sun, X., Lv, J., Ji, Y., Fu, J., Zhao, C., Yao, Y., Zhang, G., Deng, W., et al. (2024). Designing a Novel Wide Bandgap Small Molecule Guest for Enhanced Stability and Morphology Mediation in Ternary Organic Solar Cells with over 19.3% Efficiency. Adv. Sci. *11*, 2401313. https://doi.org/10.1002/advs.202401313.
15. Zhang, Z., Chen, Q., Zhang, C., Tan, W.L., Zhang, G., Bu, Z., Xiao, C., Shen, X., Tang, Z., McNeill, C.R., and Li, W. (2024). Synchronous Regulation of Donor and Acceptor Microstructure using Thiophene-Derived Non-Halogenated Solvent Additives for Efficient and Stable Organic Solar Cells. Adv. Funct. Mater. *34*, 2401823. https://doi.org/10.1002/adfm.202401823.
16. Zhou, T., Jin, W., Li, Y., Xu, X., Duan, Y., Li, R., Yu, L., and Peng, Q. (2024). Crossbreeding Effect of Chalcogenation and Iodination on Benzene Additives Enables Optimized Morphology and 19.68% Efficiency of Organic Solar Cells. Adv. Sci. *11*, 2401405. https://doi.org/10.1002/advs.202401405.
17. Ans, M., Ayub, K., Xiao, X., and Iqbal, J. (2020). Tuning Opto-Electronic Properties of Alkoxy-Induced based Electron Acceptors in Infrared Region for High Performance Organic Solar Cells. J. Mol. Liq. *298*, 111963. https://doi.org/10.1016/j.molliq.2019.111963.
18. Ans, M., Iqbal, J., Eliasson, B., saif, M.J., and Ayub, K. (2019). Opto-Electronic Properties of Non-Fullerene Fused-Undecacyclic Electron Acceptors for Organic Solar Cells. Comput. Mater. Sci. *159*, 150–159. https://doi.org/10.1016/j.commatsci.2018.12.009.
19. Li, C., Yao, G., Gu, X., Lv, J., Hou, Y., Lin, Q., Yu, N., Abbasi, M.S., Zhang, X., Zhang, J., et al. (2024). Highly Efficient Organic Solar Cells Enabled by Suppressing Triplet Exciton Formation and Non-Radiative Recombination. Nat. Commun. *15*, 8872. https://doi.org/10.1038/s41467-024-53286-2.
20. Ans, M., Ayub, A., Alwadai, N., Rasool, A., Zahid, M., Iqbal, J., and Al-Buriahi, M.S. (2022). Simultaneously Enhanced Efficiency of Eco-Friendly Structural Characterization of the Dithienocyclopentacarbazole Donor based Acceptors with Narrow Bandgap for High-Performance Organic Solar Cells. J. Phys. D Appl. Phys. *55*, 235501. https://doi.org/10.1088/1361-6463/ac53c8.
21. Khalid, M., Khan, M.U., -Razia, E.T., Shafiq, Z., Alam, M.M., Imran, M., and Akram, M.S. (2021). Exploration of Efficient Electron Acceptors for Organic Solar Cells: Rational Design of Indacenodithiophene based Non-Fullerene Compounds. Sci. Rep. *11*, 19931. https://doi.org/10.1038/s41598-021-99254-4.
22. Khan, M.U., Shafiq, F., Janjua, M.R.S.A., Khalid, M., Arshad, M., Alshehri, S.M., and Khan, R.A. (2024). Predicting Benzodithiophene based Donor Materials with Enhanced 19.09% PCE, Open-Circuit Voltage and Optoelectronic Attributes for Solar Cell Applications: Photochemical Insights

from DFT. J. Photochem. Photobiol., A *446*, 115115. https://doi.org/10.1016/j.jphotochem.2023.115115.

23. Shockley, W., and Queisser, H.J. (1961). Detailed Balance Limit of Efficiency of p-n Junction Solar Cells. J. Appl. Phys. *32*, 510–519. https://doi.org/10.1063/1.1736034.
24. Liu, J., Chen, S., Qian, D., Gautam, B., Yang, G., Zhao, J., Bergqvist, J., Zhang, F., Ma, W., Ade, H., et al. (2016). Fast Charge Separation in a Non-Fullerene Organic Solar Cell with a Small Driving Force. Nat. Energy *1*, 16089. https://doi.org/10.1038/nenergy.2016.89.
25. Liu, S., Yuan, J., Deng, W., Luo, M., Xie, Y., Liang, Q., Zou, Y., He, Z., Wu, H., and Cao, Y. (2020). High-Efficiency Organic Solar Cells with Low Non-Radiative Recombination Loss and Low Energetic Disorder. Nat. Photonics *14*, 300–305. https://doi.org/10.1038/s41566-019-0573-5.
26. Yao, J., Kirchartz, T., Vezie, M.S., Faist, M.A., Gong, W., He, Z., Wu, H., Troughton, J., Watson, T., Bryant, D., and Nelson, J. (2015). Quantifying Losses in Open-Circuit Voltage in Solution-Processable Solar Cells. Phys. Rev. Appl. *4*, 014020. https://doi.org/10.1103/PhysRevApplied.4.014020.
27. He, D., Zhao, F., Wang, C., and Lin, Y. (2022). Non-Radiative Recombination Energy Losses in Non-Fullerene Organic Solar Cells. Adv. Funct. Mater. *32*, 2111855. https://doi.org/10.1002/adfm.202111855.
28. Lüer, L., Wang, R., Brabec, C.J., Liu, C., Heumüller, T., Heumüller, T., and Hauch, J. (2024). Maximizing Performance and Stability of Organic Solar Cells at Low Driving Force for Charge Separation. Adv. Sci. *11*, 2305948. https://doi.org/10.1002/advs.202305948.
29. Chen, S., Wang, Y., Zhang, L., Zhao, J., Chen, Y., Zhu, D., Yao, H., Zhang, G., Ma, W., Friend, R.H., et al. (2018). Efficient Nonfullerene Organic Solar Cells with Small Driving Forces for Both Hole and Electron Transfer. Adv. Mater. *30*, 1804215. https://doi.org/10.1002/adma.201804215.
30. Karuthedath, S., Paleti, S.H.K., Sharma, A., Yin, H., P De Castro, C.S., Chen, S., Xu, H., Alshehri, N., Ramos, N., Khan, J.I., et al. (2023). Rationalizing the Influence of Tunable Energy Levels on Quantum Efficiency to Design Optimal Non-Fullerene Acceptor-Based Ternary Organic Solar Cells. Adv. Energy Mater. *13*, 2203464. https://doi.org/10.1002/aenm.202203464.
31. Yoshikawa, K., Kawasaki, H., Yoshida, W., Irie, T., Konishi, K., Nakano, K., Uto, T., Adachi, D., Kanematsu, M., Uzu, H., and Yamamoto, K. (2017). Silicon Heterojunction Solar Cell with Interdigitated Back Contacts for a Photoconversion Efficiency over 26. Nat. Energy *2*, 17032. https://doi.org/10.1038/nenergy.2017.32.
32. Zhan, L., Li, S., Li, Y., Sun, R., Min, J., Bi, Z., Ma, W., Chen, Z., Zhou, G., Zhu, H., et al. (2022). Desired Open-Circuit Voltage Increase Enables Efficiencies Approaching 19% in Symmetric-Asymmetric Molecule Ternary Organic Photovoltaics. Joule *6*, 662–675. https://doi.org/10.1016/j.joule.2022.02.001.
33. Gasparini, N., Salleo, A., McCulloch, I., and Baran, D. (2019). The Role of the Third Component in Ternary Organic Solar Cells. Nat. Rev. Mater. *4*, 229–242. https://doi.org/10.1038/s41578-019-0093-4.
34. Gao, J., Yu, N., Chen, Z., Wei, Y., Li, C., Liu, T., Gu, X., Zhang, J., Wei, Z., Tang, Z., et al. (2022). Over 19.2% Efficiency of Organic Solar Cells Enabled by Precisely Tuning the Charge Transfer State Via Donor Alloy Strategy. Adv. Sci. *9*, 2203606. https://doi.org/10.1002/advs.202203606.
35. Pang, S., Wang, Z., Yuan, X., Pan, L., Deng, W., Tang, H., Wu, H., Chen, S., Duan, C., Huang, F., and Cao, Y. (2021). A Facile Synthesized Polymer Featuring B−N Covalent Bond and Small Singlet-Triplet Gap for High-Performance Organic Solar Cells. Angew. Chem. Int. Ed. *60*, 8813–8817. https://doi.org/10.1002/anie.202016265.
36. Han, G., Hu, T., and Yi, Y. (2020). Reducing the Singlet−Triplet Energy Gap by End-Group $\pi-\pi$ Stacking Toward High-Efficiency Organic Photovoltaics. Adv. Mater. *32*, e2000975. https://doi.org/10.1002/adma.202000975.
37. Dou, C., Long, X., Ding, Z., Xie, Z., Liu, J., and Wang, L. (2016). An Electron-Deficient Building Block Based on the B←N Unit: An Electron Acceptor for All-Polymer Solar Cells. Angew. Chem. Int. Ed. *55*, 1436–1440. https://doi.org/10.1002/anie.201508482.
38. Zhao, R., Liu, J., and Wang, L. (2020). Polymer Acceptors Containing B←N Units for Organic Photovoltaics. Acc. Chem. Res. *53*, 1557–1567. https://doi.org/10.1021/acs.accounts.0c00281.
39. Khalid, A., Khera, R.A., Saeed, A., Khalid, M., Iqbal, S., and Iqbal, J. (2021). Designing Benzothiadiazole Based Non-Fullerene Acceptors with High Open Circuit Voltage and Higher LUMO Level to Increase the Efficiency of Organic Solar Cells. Optik *228*, 166138. https://doi.org/10.1016/j.ijleo.2020.166138.
40. Owens, D.K., and Wendt, R.C. (1969). Estimation of the Surface Free Energy of Polymers. J. Appl. Polym. Sci. *13*, 1741–1747. https://doi.org/10.1002/app.1969.070130815.
41. Flory, P.J. (1953). Principles of Polymer Chemistry (Cornell University Press).
42. Zhu, L., Zhang, M., Xu, J., Li, C., Yan, J., Zhou, G., Zhong, W., Hao, T., Song, J., Xue, X., et al. (2022). Single-Junction Organic Solar Cells with Over 19% Efficiency Enabled by a Refined Double-Fibril Network Morphology. Nat. Mater. *21*, 656–663. https://doi.org/10.1038/s41563-022-01244-y.
43. Koster, L.J.A., Smits, E.C.P., Mihailetchi, V.D., and Blom, P.W.M. (2005). Device Model for the Operation of Polymer/Fullerene Bulk Heterojunction Solar Cells. Phys. Rev. B *72*, 085205. https://doi.org/10.1103/PhysRevB.72.085205.
44. Cowan, S.R., Roy, A., and Heeger, A.J. (2010). Recombination in Polymer-Fullerene Bulk Heterojunction Solar Cells. Phys. Rev. B *82*, 245207. https://doi.org/10.1103/PhysRevB.82.245207.
45. Almora, O., Cabrera, C.I., Garcia-Cerrillo, J., Kirchartz, T., Rau, U., and Brabec, C.J. (2021). Quantifying the Absorption Onset in the Quantum Efficiency of Emerging Photovoltaic Devices. Adv. Energy Mater. *11*, 2100022. https://doi.org/10.1002/aenm.202100022.
46. Muller-Buschbaum, P. (2014). The Active Layer Morphology of Organic Solar Cells Probed with Grazing Incidence Scattering Techniques. Adv. Mater. *26*, 7692–7709. https://doi.org/10.1002/adma.201304187.

STAR★METHODS

KEY RESOURCES TABLE

REAGENT or RESOURCE	SOURCE	IDENTIFIER
Chemicals		
PM6	Solarmer	CAS:1802013-84-8
L8-BO	eFlexPV Limited (China)	CAS:2668341-40-8
PNDIT-F3N	eFlexPV Limited (China)	CAS:1800206-46-5
PEDOT:PSS (CLEVIOS^{TM} P VP AI 4083)	Heraeus	CAS:155090-83-8
Chloroform	Sigma Aldrich	CAS:865-49-6
1, 4-diiodobenzene	Sigma Aldrich	CAS:624-38-4

METHOD DETAILS

Device fabrication

The substrates with indium tin oxide (ITO) were cleaned by detergent, sonicated in deionized water and isopropanol, subsequently. After that, the clean substrates were dried in blast oven at 70°C. The ITO substrates were subjected to oxygen plasma for 5 min. An aqueous solution of PEDOT:PSS (CLEVIOS P VP AI 4083) was spin-casted onto the ITO surface at 3000 rpm for 30 s, followed by drying at 150°C for 15 min in air. The substrates were then transferred into a nitrogen-filled glove box. The donor and acceptor were dissolved in CF with 50% additive of 1, 4-diiodobenzene[3,4] by weight at the donor concentration of 7 mg mL^{-1}. The D/A ratio is 1:1.2. The blend films were subjected to thermal annealing at 90°C for 5 min. The active layers were spin-coated on substrates at 2500 rpm to give a thickness of 100 nm. Afterward, an electron transport layer of PNDIT-F3N was spin-coated from a solution (0.5 mg ml^{-1}) at a speed of 2000 rpm for 30 s. Finally, a 100 nm Ag was deposited by thermal evaporation in a vacuum chamber at a pressure of 5×10^{-6} Torr with a shadow mask.

Device characterization

The photovoltaic performance of the solar cells were measured under AM1.5G irradiation (100 mW cm^{-2}) derived from a class solar simulator (Enlitech, Taiwan), which was calibrated by a China General Certification Center-certified reference single-crystal silicon cell (Enlitech). The current density−voltage ($J-V$) curves were recorded with a Keithley 2400 source meter.

QUANTIFICATION AND STATISTICAL ANALYSIS

The data in this manuscript are shown as the means ± SD.